Coastal Engineering 156 (2020) 103624

Contents lists available at ScienceDirect

Coastal Engineering

journal homepage: http://www.elsevier.com/locate/coastaleng

CFD investigations of scour beneath a submarine pipeline with the effect of upward seepage

Yuzhu Li [a], Muk Chen Ong [a,*], David R. Fuhrman [b]

[a] Department of Mechanical and Structural Engineering and Materials Science, University of Stavanger, N-4036, Stavanger, Norway
[b] Technical University of Denmark, DK-2800, Kgs. Lyngby, Denmark

ARTICLE INFO

Keywords:
CFD
Numerical model
Submarine pipeline
Seepage
Scour

ABSTRACT

A numerical model of scour beneath subsea structures considering the effect of upward seepage in the seabed is proposed. A small seepage can cause significant changes to the hydrodynamic force on the bed surface and stability of bed particles, which can further affect the sediment transport processes and scour patterns around subsea structures. The present model is developed based on a fully-coupled hydrodynamic and morphologic sediment transport model. The unsteady Reynolds-averaged Navier-Stokes (URANS) equations are solved together with the $k-\omega$ turbulence closure. In the presence of seepage, the bed friction velocity, the bed shear stress, and the bed load transport rate will be changed as compared to conditions without seepage. The sediment particle stability is also affected and the critical Shields parameter is changed. In the presence of upward seepage forces, the repose angle of the sediment is also reduced. The present model is validated against existing experiments in terms of streamwise flow velocity distribution subjected to upward seepage. The fully-coupled hydrodynamic and morphologic model is validated against existing experiments of scour beneath a pipeline in the live-bed regime and clear-water regime, respectively. The validated model is then applied to investigate the scour development beneath a submarine pipeline subjected to different upward hydraulic gradients. It is found that the equilibrium scour width is increased with a large upward hydraulic gradient. The equilibrium scour depth stays in the range of 0.6–0.8 of the pipeline diameter for the live-bed cases. For the clear-water case, with a large upward hydraulic gradient, the equilibrium scour depth slightly decreases.

1. Introduction

Scour beneath a submarine pipeline has been investigated intensively by experiments, such as Mao (1986), Sumer and Fredsøe (1990) and Sumer and Fredsøe (1996), and numerical simulations such as Chao and Hennessy (1972), Chiew (1991), Brørs (1999), Liang et al. (2005), Fuhrman et al. (2014) and Larsen et al. (2016). The effects of current, waves and combined waves and currents on the scour pattern beneath a pipeline have been thoroughly studied. In most of the numerical studies, the seabed is regarded as an impermeable wall (Li and Cheng, 2000, 2001; Smith and Foster, 2005; Brørs, 1999; Fuhrman et al., 2014; Larsen et al., 2016) and the effect of seepage flow in the seabed on the mobility of bed particles has been ignored. In fact, the seabed soil is a porous medium. Under the effect of waves or current, seepage forces can be induced in the seabed. In certain circumstances, an upward seepage force in the seabed can cause soil liquefaction and structural instability once it exceeds the initial effective stress that exists in the seabed. A number of studies have been performed to investigate the effect of wave-induced seepage forces on the liquefaction of the seabed beneath offshore foundations or subsea structures (Ye et al., 2013; Luan et al., 2008; Li et al., 2018; Zhang et al., 2015). However, very few studies have been carried out to understand the effect of seepage in the soil on scour beneath offshore and subsea structures.

In the past decade, some studies have been carried out to investigate the change of flow structure and sediment stability in the presence of seepage in the permeable sand bed. Lu et al. (2008) reviewed the experimental studies of seepage effects on the changes of the near-bed flow velocity profile, bed shear stress and bed particle stability. Cheng and Chiew (1999) derived equations for modifying the critical shear velocity of the sand bed particles in the presence of upward seepage. Lu and Chiew (2007) conducted experiments and proposed an empirical equation for the dune dimensions and repose angles of sand particles subjected to seepage. Dey and Singh (2007) did experiments on clear-water scour depth beneath a marine pipeline with different

* Corresponding author.
E-mail address: muk.c.ong@uis.no (M.C. Ong).

https://doi.org/10.1016/j.coastaleng.2019.103624
Received 5 June 2019; Received in revised form 18 October 2019; Accepted 21 December 2019
Available online 27 December 2019

upward seepage velocities. Recently, Guo et al. (2019) did two-dimensional numerical studies on the sediment incipient motion around a free-spanning pipeline considering seepage flow in the seabed. However, the sediment transport and morphology of the seabed is not modelled in their study. So far, the scour development around subsea structures in the presence of seepage in the seabed has not been numerically modelled in any of the previous studies.

The seepage velocity inside the porous seabed is usually small compared to the free-stream velocity (Lu et al., 2008), so that it can have a minor effect on the free-stream velocity field. However, small seepage can cause a significant change to the hydrodynamic force on the bed surface. The bed friction velocity and the bed shear stress are changed. Meanwhile, upward seepage can also affect the stability of bed particles such that the threshold of incipient sediment motion, i.e., the critical Shields parameter, is also changed. Due to the decrease of the effective submerged weight of sand particles, the angle of repose is also reduced (Lu and Chiew, 2007). Therefore, the process of sediment transport, and the furthermore scour patterns, can be largely affected. In the present study, a modified numerical model of scour around a submarine pipeline, considering upward seepage effects, is proposed. The present model is based on a fully-coupled hydrodynamic and morphologic model (Jacobsen, 2011; Jacobsen et al., 2014; Jacobsen and Fredsoe, 2014). The unsteady Reynolds-averaged Navier-Stokes (URANS) equations are solved together with the $k-\omega$ turbulence closure. The same (or very similar) turbulence model has been successfully used to solve scour problems in Roulund et al. (2005), Fuhrman et al. (2014), Baykal et al. (2015), Larsen et al. (2016) and Li et al. (2020). The following modifications are implemented in order to couple seepage effects with the scouring problem.

1. In the presence of upward seepage flow, the incoming flow structure near the seabed is changed. The bed friction velocity and the streamwise velocity distribution above the seabed are modified, as discussed later in Section 2.2. The bed shear stress is reduced due to the upward seepage effect. The present model utilizes separate one-dimensional vertical (1DV) simulations driven by the body force to generate the fully-developed velocity boundary layer flow without upward seepage and then two-dimensional (2D) simulations without morphology to develop the inlet flow with upward seepage velocities until reaching equilibrium. The velocity profiles subjected to upward seepage velocities are validated against the experiments of Cheng and Chiew (1998) and Dey and Nath (2009), respectively, in Section 3.1.
2. The critical Shields parameter of bed particles in the presence of upward seepage is modified. The critical Shields parameter describes the threshold condition of sediment movement. Due to additional upward seepage forces, the critical Shields parameter is decreased, as described in Section 2.3.
3. For solving the sediment transport, the present scour model uses the bed load transport model proposed by Roulund et al. (2005). The scour model is validated against the experiments of Mao (1986) in Section 3.2. In the presence of an additional upward seepage force, the bed load transport model in Roulund et al. (2005) is modified, as discussed in Section 2.4.
4. The presence of the upward seepage will also change the repose angle of the sediment. According to Lu and Chiew (2007), with upward seepage forces, the repose angle is reduced based on the ratio of the upward hydraulic gradient i to the critical hydraulic gradient under quick conditions i_c, as discussed in Section 2.5.

Based on the considerations above, new scour profiles due to the incoming flow and the effect of upward seepage will emerge. The equilibrium scour depth and scour width with upward seepage can be different from that without upward seepage. The present modified model is applied to investigate the scour pattern around a submarine pipeline in the presence of upward seepage forces. The strength of the seepage effect is described by i/i_c, i.e., the ratio of the upward hydraulic gradient i to the critical hydraulic gradient i_c. The critical hydraulic gradient i_c describes the critical condition of liquefaction/fluidization, under which the upward seepage force just balances the submerged weight of a sand particle. If the hydraulic gradient i exceeds the critical hydraulic gradient i_c, the effective stresses between the individual grains will vanish and the fluid-sediment mixture will behave like a viscous liquid. Sumer et al. (2006) conducted experiments to investigate the sequence of sediment behaviour during wave-induced liquefaction in the soil. They found that sand ripples started to emerge only after the liquefaction and compaction process. This implies that scour does not occur during the liquefaction process, since the liquefied fluid-sediment mixture does not have a repose angle. Therefore, the present theory does not cater to fully liquefied situations. Hydraulic gradient ratios i/i_c ranging from 0 to 0.9 are thus modelled in the present numerical investigations.

2. Mathematical equations

2.1. The fully-coupled hydrodynamic and morphologic CFD model

The present numerical model incorporating upward seepage effects into scour prediction is developed based on the fully-coupled hydrodynamic and morphologic CFD model developed by Jacobsen (2011) and Jacobsen and Fredsoe (2014) in the OpenFOAM®[1] framework. The hydrodynamic model was built by solving the incompressible unsteady Reynolds-averaged Navier-Stokes (URANS) equations together with the $k-\omega$ turbulence closure (Wilcox, 2006, 2008). Detailed equations for the hydrodynamic model have been described in Jacobsen (2011), Jacobsen et al. (2014), and Fuhrman et al. (2014), and are presented in Appendix A.

The sediment transport model consists of a bed load transport model and a suspended sediment model. The bed load transport model was first proposed by Engelund and Fredsøe (1976) and extended to 3D by Roulund et al. (2005). The suspended sediment model was proposed by Fredsøe and Deigaard (1992) and described in Jacobsen (2011) in which a turbulent-diffusion equation for the concentration is solved. A full description and numerical implementation of the sediment transport model can be found in Jacobsen (2011), Jacobsen et al. (2014) and Jacobsen and Fredsoe (2014).

The morphological model for predicting the bed deformation is based on the sediment continuity (Exner) equation:

$$\frac{\partial h_b}{\partial t}=\frac{1}{1-n}\left[-\frac{\partial q_{bi}}{\partial x_i}+D_e+E\right], i=1,2 \tag{1}$$

where h_b is the bed elevation, n is the porosity which is taken as 0.4 in the present study, q_{bi} the bed load sediment transport rate in the ith direction, D_e is the deposition and E is the erosion calculated from the suspended sediment model. Further details of the computation of the bed load sediment transport rate, deposition and erosion terms are given in Jacobsen and Fredsoe (2014). To prevent the un-physical steepening of the scour hole, a sand slide model proposed by Roulund et al. (2005) is utilized in the present numerical model.

Based on the fully-coupled hydrodynamic and morphologic model as described above, the following modifications (Section 2.2 - 2.5) are implemented in order to couple seepage effects with the scouring problem.

2.2. Modified incoming flow velocity distribution subjected to upward seepage

For a two-dimensional flow over a horizontal impermeable rough

[1] OpenFOAM® is a registered trademark of OpenCFD Ltd.

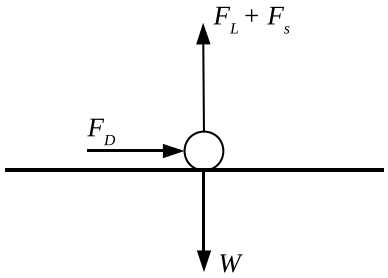

Fig. 1. Two-dimensional force balance on a single moving particle on a flat bed.

bed without seepage, the vertical distribution of streamwise velocity can be expressed as:

$$\frac{u}{u_f}=\frac{1}{\kappa}\left(\ln\left(\frac{30y}{k_s}\right)\right) \tag{2}$$

where u is the streamwise flow velocity, $u_f=\sqrt{\tau_b/\rho}$ is the friction velocity, τ_b is the wall shear stress, ρ is the fluid density, $\kappa=0.4$ is the von Karman constant, $k_s=2.5d$ is Nikuradse's equivalent sand roughness, d is the median grain diameter.

When upward seepage is applied to an open-channel flow, the resulting velocity distribution over a flat bed is expressed with a modifed logarithmic law derived in Cheng and Chiew (1998):

$$\frac{u}{u_f}=\frac{1}{\kappa}\ln\left(\frac{30y}{k_s}\right)+\frac{v_s}{4u_f}\left(\frac{1}{\kappa}\ln\left(\frac{30y}{k_s}\right)\right)^2 \tag{3}$$

where v_s is the upward seepage flow velocity.

In the present numerical model, the friction velocity u_f is determined from the tangential velocity at the nearest cell center based on the modified logarithmic velocity distribution:

$$u_f=\frac{u_{y_c}-\frac{v_s}{4}\left(\frac{1}{\kappa}\ln\left(\frac{30y_c}{k_s}\right)\right)^2}{\frac{1}{\kappa}\ln\left(\frac{30y_c}{k_s}\right)} \tag{4}$$

where u_{y_c} is the streamwise velocity at the level of y_c without seepage, $y_c=\Delta y/2$ is the normal distance from the wall to the first cell center. The friction velocity is utilized based on standard wall functions for k and ω in the first layer of the cells nearest to the wall (Wilcox, 2006, 2008).

$$k=\frac{(u_f)^2}{\sqrt{\beta^*}} \tag{5}$$

$$\omega=\frac{u_f}{\sqrt{\beta^*}\kappa\Delta y} \tag{6}$$

where $\beta^*=0.09$ is the standard closure coefficient. Detailed equations for the present hydrodynamic model are presented in Appendix A. Equation (4) indicates that the friction velocity at the seabed with the upward seepage is reduced compared to the friction velocity at the seabed without the upward seepage. In the present work, the incoming flow velocity profile and the friction velocity subjected to upward seepage effects are computed via 1DV and 2D simulations and are validated in Section 3.1.

2.3. Modified incipient sediment motion equation subjected to upward seepage

Assuming the bed load particle as a sphere, the forces acting on the particle on a flat bed consist of the effective weight force W, the flow-induced drag force F_D, the flow-induced lift force F_L, and the upward seepage force F_S, as shown in Fig. 1. The direction of the upward seepage flow is assumed normal to the bed surface such that the seepage force acts in the same direction as the lift force. The equations of each force are expressed as follows:

$$W=\frac{1}{6}\pi(s-1)\rho g d^3 \tag{7}$$

$$F_D=C_D\frac{\pi d^2}{8}\rho u_r^2 \tag{8}$$

$$F_L=C_L\frac{\pi d^2}{8}\rho u_r^2 \tag{9}$$

where C_D and C_L are the drag and lift coefficients, s is the relative sediment density, ρ is the density of fluid, d is the mass median diameter of sediment particles, and g is the gravitational acceleration, u_r is the velocity of the flow (at the particle position) relative to that of the bed load particle. For a 2D case, the relative velocity u_r directly relates to the shear friction velocity u_f, according to Chiew and Parker (1994).

$$u_r=\frac{u_f}{\sqrt{f_*}} \tag{10}$$

where f_* is a form of friction factor.

The seepage force normal to the bed surface F_S is expressed as (Cheng and Chiew, 1998)

$$F_S=\frac{i\rho g\pi d^3}{6(1-n)} \tag{11}$$

where n is the porosity. The seepage force acting on a porous medium per unit volume is expressed as $S=i\rho g$ (Bear, 2013). The number of sediment particles per unit volume is expressed as $N=\frac{1-n}{\pi d^3/6}$ (Cheng and Chiew, 1999). S/N yields the seepage force on a single particle in Eqn. (11).

On a flat bed with an upward seepage force, the force balance at incipient sediment motion can be written as

$$F_D-(W-F_L-F_S)\tan\varphi_s=0 \tag{12}$$

where φ_s is the repose angle of the sediment particles, and $\tan\varphi_s$ is equal to the static friction velocity μ_s.

Substituting Eqns. (7)–(11) into Eqn. (12), the critical friction velocity at incipient sediment motion can be expressed as

$$\frac{u_f^2}{f_*(s-1)gd}=\frac{\frac{4}{3}\left[1-\frac{i}{(s-1)(1-n)}\right]}{C_L+C_D/\tan\varphi_s}=\frac{\frac{4}{3}\left(1-\frac{i}{i_c}\right)}{C_L+C_D/\tan\Phi_s} \tag{13}$$

where $i_c=(s-1)(1-n)$ is the aforementioned critical hydraulic gradient which describes the critical condition of liquefaction/fluidization of the sand bed sediments.

The action of flow on the bed can be measured by a dimensionless form of the shear stress, the Shields parameter θ, expressed as

$$\theta=\frac{u_f^2}{(s-1)gd} \tag{14}$$

The critical Shields parameter $\theta_{c0}=\frac{u_{fc}^2}{(s-1)gd}$ describes the threshold condition of incipient sediment motion on the flat bed.

Therefore, the critical Shields parameter on the horizontal flat bed with seepage is expressed as

$$\theta_{c0}=\frac{\frac{4}{3}\left(1-\frac{i}{i_c}\right)f_*}{C_L+C_D/\tan\varphi_s} \tag{15}$$

If we consider the incipient motion equation without seepage, i.e. $i=$

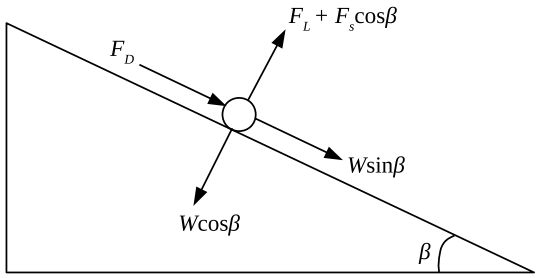

Fig. 2. Two-dimensional force balance on a single moving particle on a sloping bed.

0, the equation for critical Shields parameter $\theta_{c0,i=0}$ is:

$$\theta_{c0,i=0} = \frac{\frac{4}{3}f_*}{C_L + C_D/\tan\varphi_s} \tag{16}$$

Combining Eqn. (15) and Eqn. (16), the relation between the critical Shields parameters with and without the seepage force is

$$\frac{\theta_{c0}}{\theta_{c0,i=0}} = 1 - \frac{i}{i_c} \tag{17}$$

It is noted that f_* has been eliminated in Eqn. (17).

Now, we consider the force balance with upward seepage on a sloping bed, as shown in Fig. 2.

On a sloping bed of angle β, the force balance at incipient sediment motion can be written as

$$W\sin\beta + F_D = (W\cos\beta - F_L - F_S\cos\beta)\tan\varphi_s \tag{18}$$

where φ_s is again the repose angle of the sediment particles, and $\tan\varphi_s$ is again equal to the static friction coefficient μ_s. Substituting Eqns. (7)–(11) into Eqn. (18), the critical Shields parameter on a sloping bed with upward seepage force is expressed as

$$\theta_c = \frac{\frac{4}{3}\left[\cos\beta - \frac{\sin\beta}{\tan\varphi_S} - \frac{i\cos\beta}{(s-1)(1-n)}\right]f_*}{C_L + C_D/\tan\varphi_s} \tag{19}$$

Combining Eqn. (15) and Eqn. (19), the slope correction of the critical Shields parameter with upward seepage force is written as

$$\frac{\theta_c}{\theta_{c0}} = \cos\beta - \frac{\frac{\sin\beta}{\tan\varphi_S}}{1 - \frac{i}{i_c}} \tag{20}$$

2.4. Modified bed load transport model subjected to upward seepage

The present bed load transport model is based on Roulund et al. (2005) which is a generalized 3D extension of the transport formulation proposed by Engelund and Fredsøe (1976). The 3D force balance equations for the bed load transport is simplified to 2D in the present study. An additional upward seepage force is added in the force balance equations.

The forces acting on the particle consist of the agitating forces and the stabilizing forces (Fredsøe and Deigaard, 1992). The agitating forces include the gravity in the slope direction $W\sin\beta$ and the flow-induced drag and lift forces. In the model of Engelund and Fredsøe (1976), the drag and lift forces are considered as one force with the same direction as u_r, which is given by

$$F_{D,L} = \frac{1}{2}\rho c\frac{\pi}{4}d^2u_r^2 \tag{21}$$

The empirical equation of the coefficient $c = C_D + \mu_d C_L$ is (Fredsøe and Deigaard, 1992)

$$c = \frac{4\mu_s}{3a^2(\theta_{c0}/2)} \tag{22}$$

where μ_d is the dynamic friction coefficient, here taken as 0.51, following Fredsøe and Deigaard (1992) and a is an empirical constant taken as 10 according to Engelund and Fredsøe (1976) and Roulund et al. (2005).

The stabilizing force is the friction force that acts in the direction opposite to the particle motion, which was $\mu_d W\cos\beta$ in the original formulation in Engelund and Fredsøe (1976). In the presence of the upward seepage force, the stabilizing force is modified to $\mu_d(W - F_s)\cos\beta$.

Therefore, the modified dynamic force balance equation on a sloping bed is written as

$$F_{D,L} + W\sin\beta = \mu_d(W - F_s)\cos\beta \tag{23}$$

The relation between u_r and the bed load transport velocity u_b is given by

$$u_r = a\cdot u_f - u_b \tag{24}$$

According to Engelund and Fredsøe (1976), the bed load sediment transport rate q_b can be written as

$$q_b = \frac{\pi}{6}d^3\frac{p_{EF}}{d^2}u_b \tag{25}$$

u_b is solved by Eqn. (23) and Eqn. (24). p_{EF} is the percentage of particles in motion in the surface layer of the bed, and is expressed by Engelund and Fredsøe (1976):

$$p_{EF} = \left[1 + \left(\frac{\frac{1}{6}\pi\mu_d}{\theta - \theta_c}\right)^4\right]^{-1/4} \tag{26}$$

θ is the computed Shields parameter according to Eqn. (14), and θ_c is the critical Shields parameter with the upward seepage and slope corrections, according to Eqn. (17) and Eqn. (20).

2.5. Angle of repose

Lu and Chiew (2007) inspected the influence of seepage on the critical slope of sediment. They found that the repose angle of the sediment is reduced with injection and is increased with suction. In the present work, the empirical equation derived by Lu and Chiew (2007) is used to predict the critical slope (angle of repose) of the sediment subjected to upward seepage:

$$\frac{i}{i_c} = C_s\sin(\varphi_{s0} - \varphi_s) \tag{27}$$

where C_s is the coefficient related to the sediment properties, φ_{s0} and φ_s are the repose angle of the sediment without and with upward seepage. In the present simulations, $\varphi_{s0} = 34^\circ$ and $C_s = 2.63$ are adopted based on the study of Lu and Chiew (2007).

3. Validations

3.1. Validation of boundary layer velocity profile with seepage

When upward seepage is applied to an open-channel flow, the resulting streamwise velocity profile in the boundary layer is changed. Cheng and Chiew (1998) and Dey and Nath (2009) conducted experiments of flow propagating over the immobile rough bed in wave tanks and measured the vertical velocity distributions subjected to the upward seepage velocities. Two of their experiments are reproduced using the present numerical model with the $k-\omega$ turbulence closure to validate the incoming flow simulation in the present work.

The experiment of Dey and Nath (2009) was conducted in a wave flume which is 0.6 m wide, 0.71 m deep and 12 m long. In their experiment, a seepage zone of 2 m long, 0.6 m wide was placed at 7.5 m

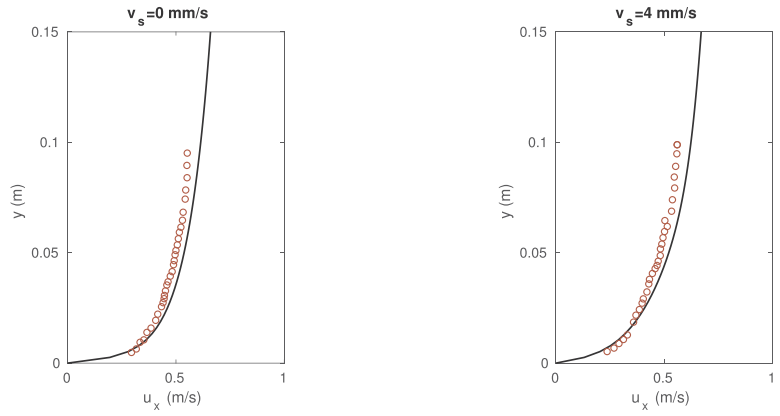

(a) Vertical profiles of streamwise velocity with v_s=0. (b) Vertical profiles of streamwise velocity with v_s=4 mm/s.

Fig. 3. Vertical profiles of streamwise velocity measured at the location where flows traveled 1.2 m over the seepage zone. The seepage zone was placed at 7.5 m downstream from the inlet. The flows in the experiments were not fully-developed, yielding a different u_f from that in the present numerical simulation where the flows are fully-developed. Therefore, the plots here are dimensional in stead of normalized by u_f. –: Present numerical simulations; ∘: Experimental measurement by Dey and Nath (2009).

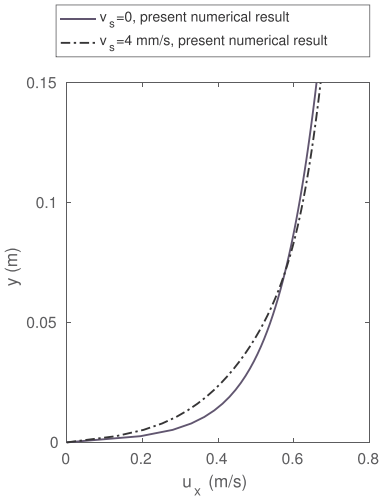

Fig. 4. Comparison of vertical profiles of streamwise velocity without and with upward seepage (numerical reproduction of the experiment of Dey and Nath (2009)).

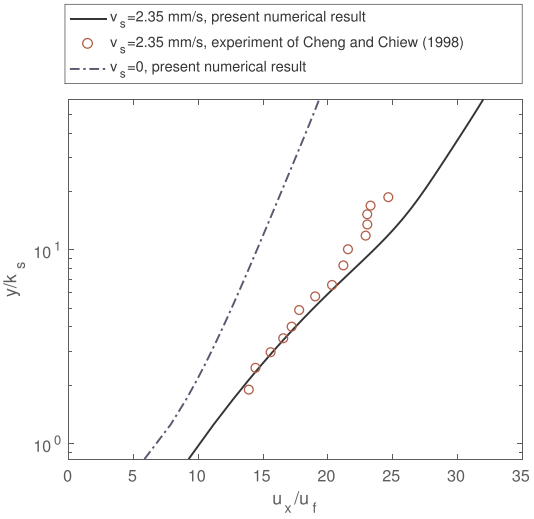

Fig. 5. Vertical profiles of streamwise velocities u_x with and without seepage, normalized by their friction velocities at the bed u_f. The data are measured at the location where flows traveled 1 m over the seepage zone. The seepage zone was placed at 16 m downstream from the inlet. An upward seepage velocity $v_s = 2.35$ mm/s was applied in the experiment of Cheng and Chiew (1998).

downstream from the inlet. A uniform gravel layer was placed at the tank bottom and the seepage kit surface to achieve the same roughness. The gravel sediments had a median size of $d_{50} = 4.1$ mm and a relative density of $s = 2.65$. The velocity profile was measured at the location where flows traveled 1.2 m over the seepage zone. The measured depth-averaged streamwise velocity was 0.555 m/s and the flow depth was 0.15 m. The upward seepage velocity through the gravel-layer was 4 mm/s and was uniformly distributed within the gravel layer. The roughness Reynolds number $k_s^+ = \frac{k_s u_f}{\nu}$ in their experiments was $k_s^+ = 338$ for $v_s = 0$ and $k_s^+ = 317$ for $v_s = 4$ mm/s. In the present numerical simulation, a 2D numerical wave tank is modelled. The top boundary of the tank is treated as a frictionless slip wall where the vertical velocity component is zero. The outlet boundary is specified with zero normal velocity gradient and zero pressure. First, a one-dimensional vertical (1DV) simulation driven by the body force is conducted to achieve a fully-developed velocity profile without the seepage effect. The body force is $F = \frac{u_f^2}{h}$, where u_f is the desired friction velocity without the seepage and h is the height of the numerical wave tank. In the simulations, the smallest cells near the tank bottom have a height of $0.3k_s$. Next, after the 1DV flow is fully-developed, the u, k and ω fields are applied as the boundary conditions for the inlet in the 2D simulation. The 2D wave tank is 2 m long and 0.71 m deep. An upward seepage velocity $v_s = 4$ mm/s is set at the tank bottom. The flows eventually reach a new equilibrium state, with a reduced friction velocity. The final vertical profile of the streamwise velocity in the 2D numerical wave tank with upward seepage is compared with the experimental data of Dey and Nath (2009) measured at the centerline of the flume (i.e., with equal horizontal distance to the two lateral sides of the tank). As seen in Fig. 3a, a reasonable agreement is achieved between the present numerical simulation and the experimental measurements. The minor discrepancy may be because in the experiment of Dey and Nath (2009), the flow was not fully-developed before reaching the seepage zone. The vertical profiles of streamwise velocity with and without seepage velocity produced by the present numerical simulations are compared in Fig. 4. It is seen that with the upward seepage, the streamwise flow velocity close to the bed is reduced and the bed friction velocity decreases. The vertical profile of the streamwise velocity shifts up.

Cheng and Chiew (1998) have conducted a similar experiment in a 30 m long, 0.7 m wide and 0.6 m deep wave flume. In their experiment, the seepage zone was located 16 m from the inlet, to allow the incoming flow to be fully developed. The seepage zone was 2.0 m long. They conducted a series of experiments to validate the proposed empirical equation for the vertical profile of the streamwise velocity, as given in

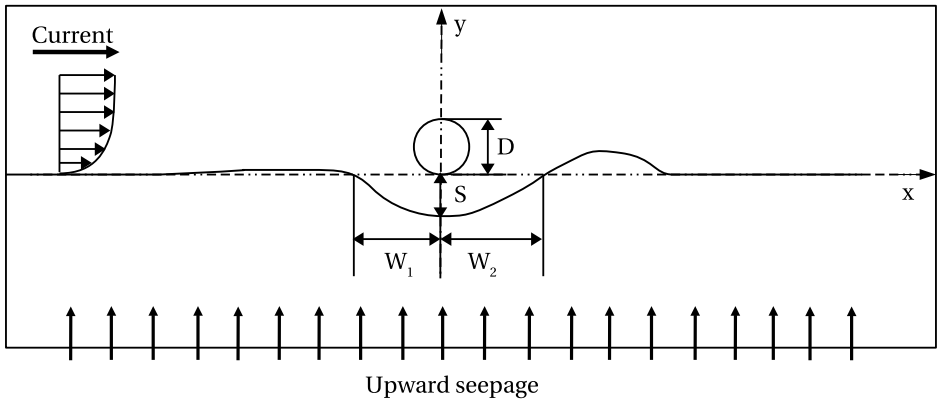

Fig. 6. Layout of the present numerical simulations of scour beneath a pipeline in current and upward seepage.

Table 1
Parameters in the present simulations for the live-bed scour and the clear-water scour with upward hydraulic gradients.

$i/\ i_c$	0	0.1	0.2	0.3	0.4	0.5	0.6	0.7	0.8	0.9
$v_s = Ki$ cm/s	0	0.0099	0.0198	0.0297	0.0396	0.0495	0.0594	0.0693	0.0792	0.0891
Live-bed cases										
Desired u_f m/s	0.0174	0.0169	0.0165	0.016	0.0156	0.0151	0.0147	0.0142	0.0138	0.0133
Far-field θ	0.098	0.093	0.0881	0.0833	0.0787	0.0742	0.0698	0.0655	0.0614	0.0575
Repose angle φ_s	34	31.82	29.64	27.45	25.25	23.04	20.81	18.56	16.29	13.99
θ_{cr0}	0.045	0.0405	0.036	0.0315	0.027	0.0225	0.018	0.0135	0.009	0.0045
Clear-water cases										
Desired u_f m/s	0.0122	0.0117	0.0113	0.0108	0.0103	0.0099	0.0094	0.0090	0.0085	0.0081
Far-field θ	0.048	0.0445	0.0411	0.0379	0.0348	0.0318	0.0290	0.0263	0.0237	0.0212
Repose angle φ_s	34	31.82	29.64	27.45	25.25	23.04	20.81	18.56	16.29	13.99
θ_{cr0}	0.05	0.045	0.04	0.035	0.03	0.025	0.02	0.015	0.01	0.005

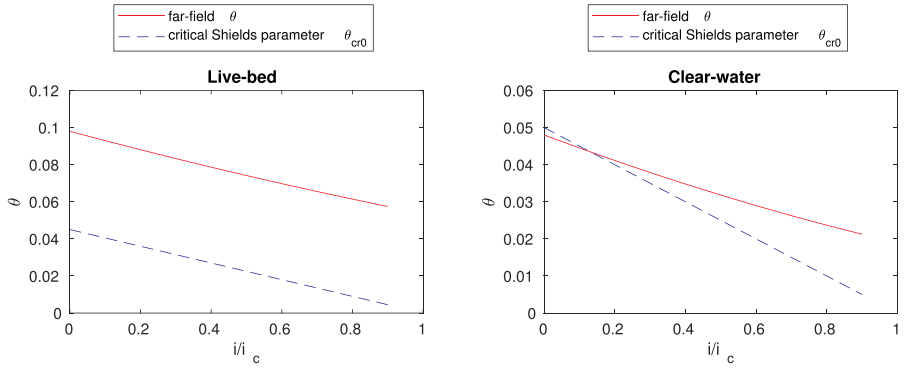

(a) The initial case with $i/i_c = 0$ is in the live-bed regime. (b) The initial case with $i/i_c = 0$ is in the clear-water regime.

Fig. 7. Far-field θ and critical Shields parameter θ_{cr0}.

Eqn. (3). The present work reproduced one of their experiment with sediments of $d_{50} = 1.95$ mm and $s = 2.65$. The velocities are measured at 1 m upstream of the beginning of the seepage zone. The depth-averaged streamwise velocity was 0.36 m/s and the flow depth was 0.148 m. The upward seepage velocity at the seepage zone surface is 2.35 mm/s. The roughness Reynolds number in their experiments was $k_s^+ = 120$ for $v_s = 0$ and $k_s^+ = 84$ for $v_s = 2.35$ mm/s. The non-dimensional plots of the vertical distributions of the streamwise velocity from the present numerical simulation and the experiment are compared in Fig. 5. The present numerical result is in good agreement with the measurements reported by Cheng and Chiew (1998). A minor discrepancy is observed at the location further away from the bed. This may be because in the experiment the limited width of the tank generated a secondary flow in the transverse direction near to the free surface. However, the secondary flow effect does not exist in the numerical simulation since the numerical wave tank is 2D, assuming that there is no wall effect of the lateral sides.

3.2. Validation of the scour model

The present scour model has been validated in Larsen et al. (2016) against the experiments conducted by Mao (1986) involving scour beneath a submarine pipeline in the clear-water regime and live-bed regime, respectively. The far-field Shields parameter θ is 0.048 for the clear-water scour and 0.098 for the live-bed scour. No upward seepage was applied in the experiments.

In the experiments of Mao (1986), the pipeline diameter was $D = 0.1$ m and the grain size was $d = 0.36$ mm. In the present numerical simulations and in Larsen et al. (2016), the pipeline diameter and grain size were set to $D = 0.03$ m and $d = 0.19$ mm, in order to reduce the

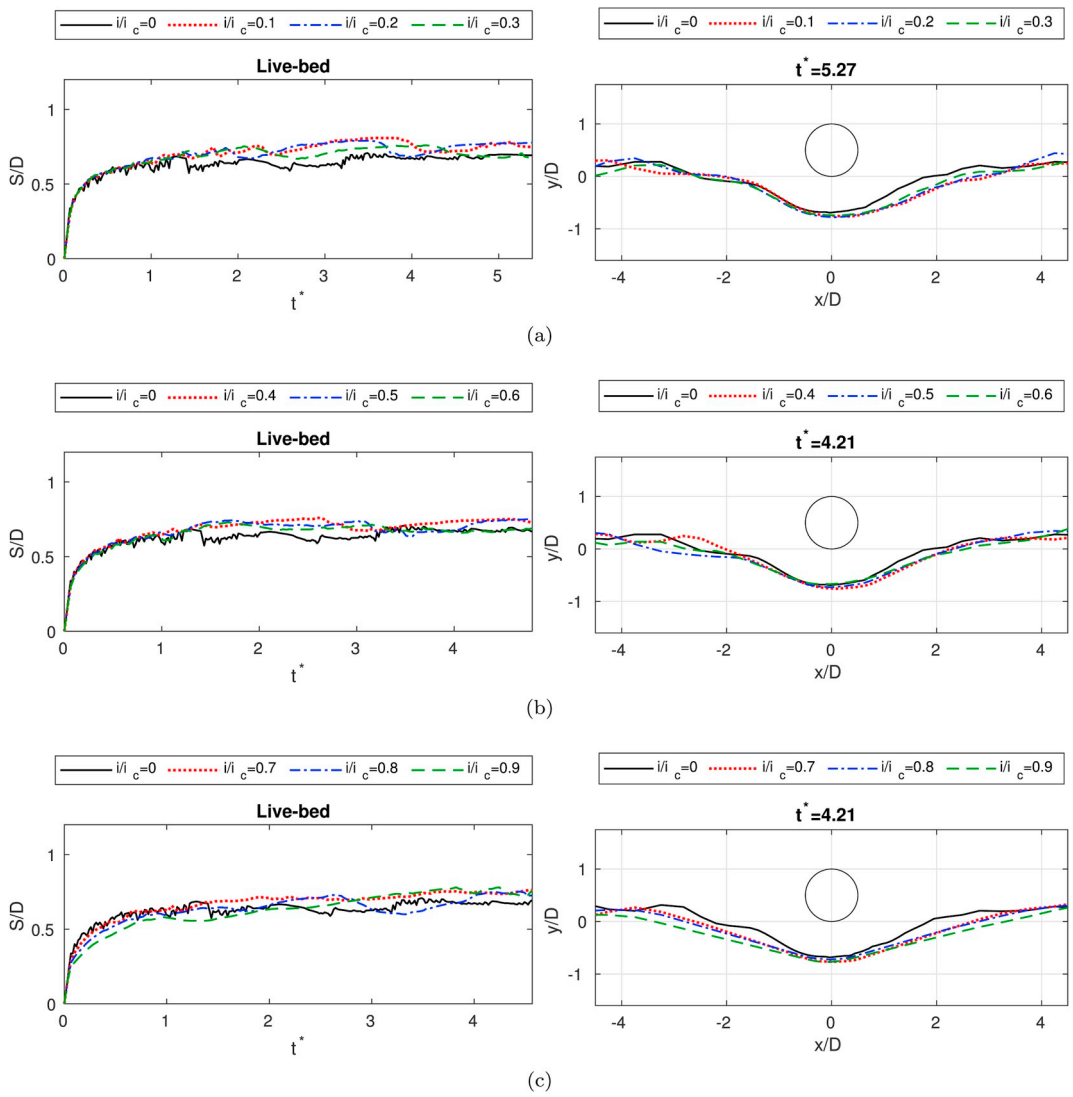

Fig. 8. Numerical results of scour depth development and scour profiles for the live-bed scour with upward hydraulic gradients.

numerical domain size and to save computational costs. The far-field friction velocity u_f is calculated using Eqn. (14) and is equal to 0.012 m/s for the clear-water scour case and 0.017 m/s for the live-bed scour case. Following the discussion in Larsen et al. (2016), it is comparable in terms of the non-dimensional scour developments between two different scales once the Shields parameter is kept the same. The comparison between the numerical simulations in Larsen et al. (2016) and the experiment of Mao (1986) was performed in terms of S/D over the non-dimensional time t^* defined as

$$t^* = \frac{\sqrt{g(s-1)d^3}}{D^2}t \tag{28}$$

where t is the physical time. Validation studies against experiments of Mao (1986) have also been repeated as a preliminary study in the present work, similar to those made (using the same model) in Larsen et al. (2016). Good agreement between the numerical results and the experimental data has been obtained. As these results are essentially the same as those shown in Larsen et al. (2016), they are not shown here for the sake of brevity.

4. Scour beneath the pipeline with upward seepage

4.1. Numerical setup

The present work investigates the effect of upward seepage on scour beneath a pipeline in the live-bed regime and clear-water regime, respectively. The layout of the numerical simulations is presented in Fig. 6. The inlet and outlet are located with a distance of 20D to the pipeline center. The height of the wave tank is 10D. The present work utilizes the same 2D mesh as in Fuhrman et al. (2014) for modeling scour beneath a submarine pipeline. An initial hole of $S_0/D = 0.15$ is specified in the numerical simulations. The pipeline diameter in the present simulations is 0.03 m. The grain size is $d = 0.19$ mm. The specific gravity of the sediment grains is $s = 2.65$. The repose angle of the sediment is 34°. Because of the initial hole in the numerical mesh, an approximation time $t_0 = \frac{S_0/D}{dS/dt}$ is added to the beginning of the time series for the development of the initial scour hole. dS/dt is calculated by the scour depth growth during the initial two saved time instants divided by the saved time step. For the present simulations, the simulation results are saved every 3 s, i.e., $\Delta t^* = 0.035$.

The investigations are performed based on the numerical cases of scour without the seepage effect, i.e., the live-bed scour case ($\theta = 0.098$) and the clear-water scour case ($\theta = 0.048$) of Mao (1986) in the

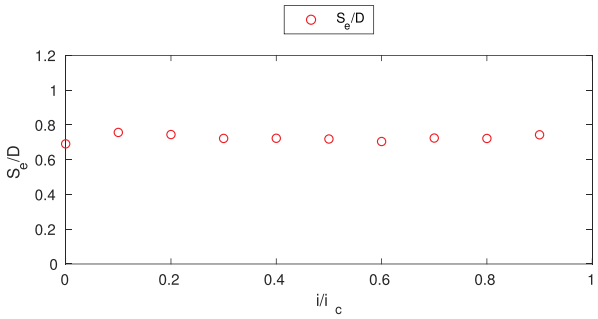

(a) Equilibrium scour depth with upward hydraulic gradients in the live-bed regime.

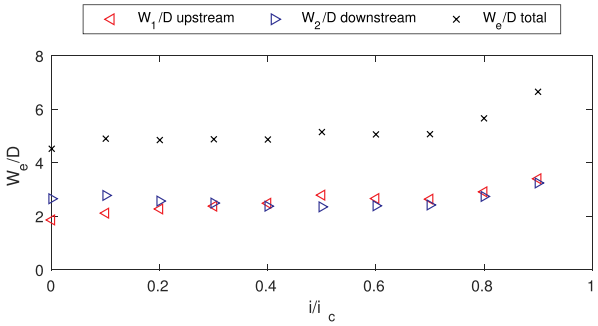

(b) Equilibrium scour width with upward hydraulic gradients in the live-bed regime.

Fig. 9. Equilibrium scour depth and width with upward hydraulic gradients in the live-bed regime.

validation study in Section 3.2. The critical Shields parameter θ_{c0} is set as 0.045 for the live-bed scour and 0.05 for the clear-water scour in the present numerical simulations. To investigate the effect of upward seepage on scour beneath a pipeline, nine levels of upward hydraulic gradients ($i/i_c = 0.1, 0.2, 0.3, \ldots, 0.9$) are applied to the live-bed scour case and the clear-water scour case, respectively.

The relationship between the upward hydraulic gradient i and the seepage velocity v_s can be derived by Darcy's law (Bear, 2013) when the seepage flow through the porous bed is linear, i.e., the seepage velocity v_s is proportional to the hydraulic gradient i:

$$v_s = Ki \tag{29}$$

where K is the permeability of the sand bed. However, it is noted that Darcy's law neglects the kinetic energy of the pore water. Therefore, it is feasible for the porous seabed consisting of fine sand where the kinetic energy of the seepage flow is insignificant and the seepage flow is within the laminar regime (Cheng and Chiew, 1999). In the present study, fine sand with a grain size of 0.19 mm and a permeability K of 0.001 m/s is considered. Darcy's law is applied for the relationship between i and v_s.

Meanwhile, in the presence of various levels of $i/\ i_c$, the desired friction velocity at the bed (Eqn. (4)), the critical Shields parameter (Eqn. (17)) and the angle of repose (Eqn. (27)) are changed when subjected to upward seepage. The parameters in the present numerical cases are presented in Table 1.

According to Eqn. (17), with the upward seepage, the critical Shields parameter will be reduced. In certain circumstances, as the upward seepage increases, the initial clear-water condition may turn to a live-bed condition, such as clear-water cases with $i/i_c = 0.4$–0.9 in Table 1, i.e., the far-field Shields parameter exceeds the critical Shields parameter. The far-field θ and critical Shields parameter θ_{cr0} for live-bed cases and clear-water cases are plotted in Fig. 7a and b, respectively. For the clear-water cases with $i/i_c = 0.2$ and 0.3, θ is just slightly higher than θ_{cr0}. These two cases are still resembling clear-water cases. In the present work, although some of the clear-water cases subjected to large upward hydraulic gradients have transformed to the live-bed regime, they are discussed within the clear-water regime in the present study in order to compare with the initial condition without the seepage effect. This regime change is, in fact, a potentially important effect of seepage.

To simulate an accurate flow field in the parametric studies with different upward seepage velocities, first, the 1DV simulation driven by the body force is computed to generate a fully developed velocity boundary layer profile without seepage. Second, in the 2D simulations of scour beneath a submarine pipeline, a Dirichlet boundary is specified with time-varying u, k and ω, taken from the preliminary 1DV simulations. The morphology is switched off to run the pure flow for a duration of $t = 20L/u$ until the flow propagating in the whole domain reaches equilibrium. Here, L is the domain length and u is the free stream velocity at the pipeline center. At the third step, the upward seepage velocity v_s is added at the bottom boundary to run the pure flow for another $t = 20L/u$. Finally, when the flow field is well-developed, the morphology is switched on and the scour hole begins to develop.

4.2. Live-bed scour with upward seepage

For live-bed cases with upward seepage, the time series of the non-dimensional scour depth S/D beneath the center of the pipeline and the scour profiles at the equilibrium stages are presented in Fig. 8. It is seen in Fig. 8a and b that with small and medium upward hydraulic gradients, i.e., $i/i_c = 0.1$–0.6, the patterns of the time series curves S/D are very similar to that with $i/i_c = 0$. The time it takes to reach the equilibrium status is almost the same among the cases with $i/i_c = 0.1$–0.6. After reaching the equilibrium stage, the scour profiles with upward seepage have slightly larger depths below the center of the pipeline compared to those without upward seepage. Also, larger scour widths are observed both upstream and downstream of the pipeline. Fig. 8c shows the time series and scour profiles with large upward hydraulic gradients, i.e., $i/i_c = 0.7$–0.9. It is seen in the left column of Fig. 8c that during the early stage of the scour development, the cases with a larger i/i_c have an obviously smaller S/D. However, after reaching equilibrium, the scour depths with $i/i_c = 0.7$–0.9 reach a similar value as with $i/i_c = 0$.

The equilibrium scour depth and scour width are calculated based on data of 180 s time duration in the equilibrium stage (non-dimensional time duration $t^* = 2.1$). The average upstream scour width W_1/D and the downstream scour width W_2/D are calculated and the total scour width is calculated as $W_e/D = \frac{W_1+W_2}{D}$. W_1 and W_2 are the horizontal distances from the center of the pipeline to the end of the scour hole, as shown in Fig. 6. The equilibrium scour depths with i/i_c from 0 to 0.9 are shown in Fig. 9a and the equilibrium scour widths are shown in Fig. 9b. It is observed that with upward hydraulic gradients, the equilibrium scour depths in the live-bed regime are still distributed in the range of $S_e/D = 0.6$ to 0.8 (in the live-bed regime without the upward seepage, the empirical relation is $S_e/D = 0.6 \pm 0.2$ (Sumer and Fredsøe, 2002)). Fig. 9b shows that with small and medium upward hydraulic gradients, i.e., $i/i_c = 0.1$–0.6, the total scour widths are similar and only slightly larger than that with $i/i_c = 0$. As the upward hydraulic gradient increases from 0.7 to 0.9, the scour width increases dramatically. As also seen in the scour profile in Fig. 8c, the final scour profile has a much wider and milder slope because of the decrease of the repose angle in a large upward hydraulic gradient. It is also observed in Fig. 9b that, as i/i_c increases, the upstream scour width W_1/D generally increases. W_1/D is smaller than W_2/D with small i/i_c but is almost the same as W_2/D with large i/i_c.

4.3. Clear-water scour with upward seepage

For the clear-water cases with the upward seepage, the time series of S/D beneath the center of the pipeline and the scour profiles at the equilibrium stages are presented in Fig. 10. It is shown that with a relatively small i/i_c, i.e., $i/i_c =$ 0.1–0.4, the S/D after reaching

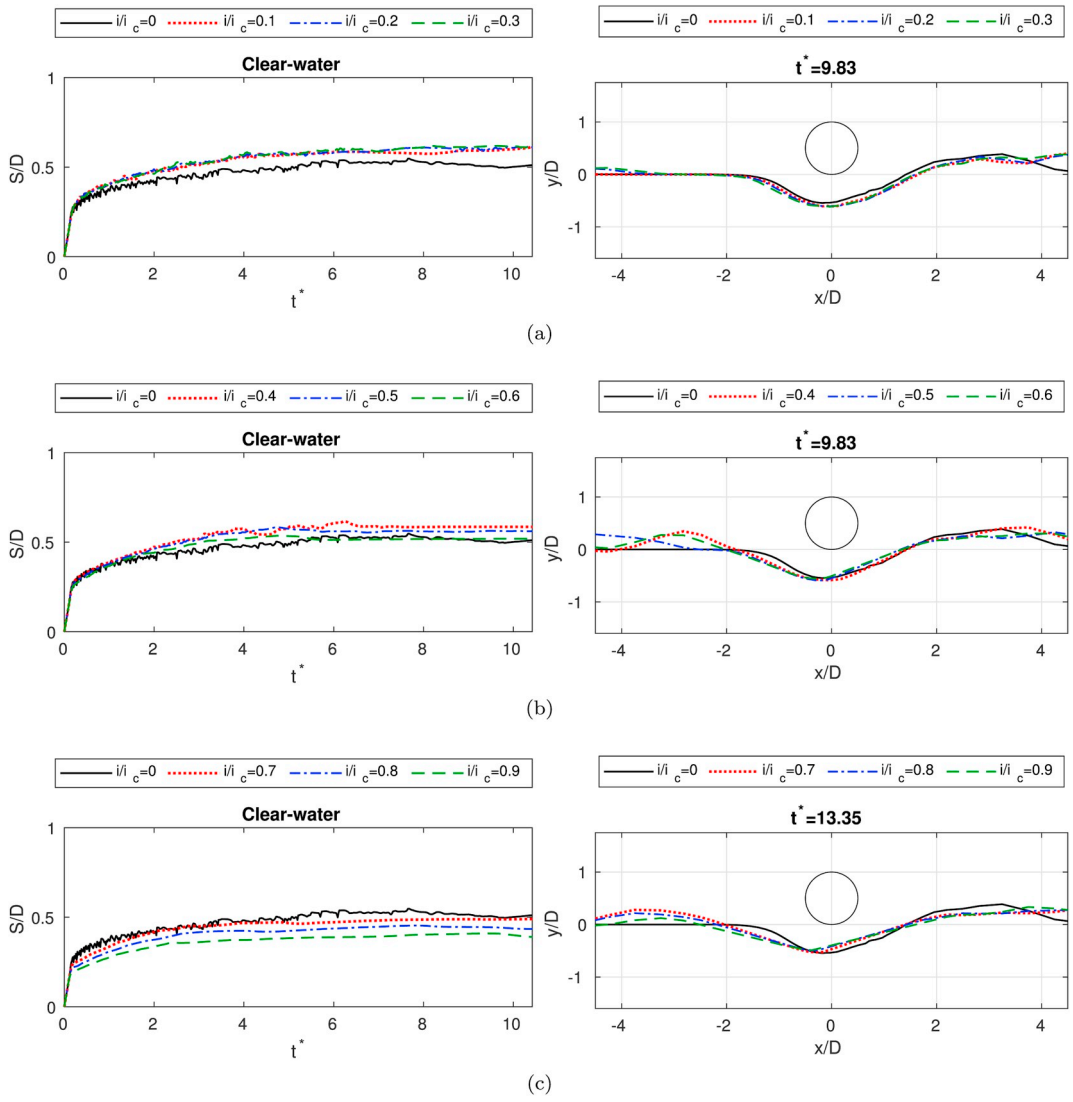

Fig. 10. Numerical results of scour depth development and scour profiles for the clear-water scour with upward hydraulic gradients.

equilibrium is slightly larger than that with $i/i_c = 0$. However, with $i/i_c = 0.5$–0.9, the S/D after reaching equilibrium is smaller than that with $i/i_c = 0$. As i/i_c increases from 0.5 to 0.9, S/D decreases. It is observed in the scour profiles in Fig. 10c that with $i/i_c = 0.7$–0.9, the location of maximum scour moves slightly upstream with larger upward hydraulic gradients. Fig. 11a shows the equilibrium scour depth S_e/D beneath the center of the pipeline and also the maximum S_e/D beneath the pipeline. It appears that both S_e/D beneath the center of the pipeline and the maximum S_e/D decrease as i/i_c increases from 0.4 to 0.9. As i/i_c increases, the location of the maximum S_e/D moves more upstream so that the difference between the S_e/D beneath the center of the pipeline and the maximum S_e/D increases. This is because the far-field Shields parameter is small for the original clear-water case. With a large upward hydraulic gradient, the bed friction velocity becomes even smaller. Therefore, the downstream sediment cannot be washed away from the scour hole.

Fig. 12 shows a comparison of the near-bed velocity field between the live-bed case and the clear-water case with $i/i_c = 0.9$. It is seen that at a relatively early stage of scour development ($t^* = 1.74$ for the live-bed case and $t^* = 3.74$ for the clear-water case), both the live-bed and the clear-water cases have a maximum scour depth slightly upstream of the pipeline center. This is due to the reduced repose angle with $i/i_c = 0.9$ so that sediments downstream slide down into the scour hole. However, since the live-bed case has a relatively high bed friction velocity, the downstream sediments are eventually washed away and the maximum scour depth moves to below the center of the pipeline. The vertical profiles of the horizontal velocity close to the seabed at $x/D = 2.67$ for the live-bed and the clear-water cases with $i/i_c = 0.9$ are compared in Fig. 13. It is seen in both Figs. 12b and 13 that the bed-friction velocity for the clear-water case with $i/i_c = 0.9$ is so small compared to the live-bed case that it is not capable of transporting sediments upward along the downstream slope out from the scour hole.

The equilibrium scour widths for the clear-water cases with upward hydraulic gradients are presented in Fig. 11b. Similar to the live-bed cases, the scour widths for the clear-water cases with small and medium upward hydraulic gradients ($i/i_c = 0.1$–0.6) are similar, with a slightly increasing trend. As the upward hydraulic gradient increases from 0.6 to 0.9, the scour width has an obvious increasing trend. The upstream scour width generally increases with i/i_c, while the downstream scour width remains almost the same.

5. Conclusions

The present study has proposed a numerical model of scour beneath subsea structures considering the upward seepage effect in the seabed. Subjected to upward seepage, the bed friction velocity and the bed shear

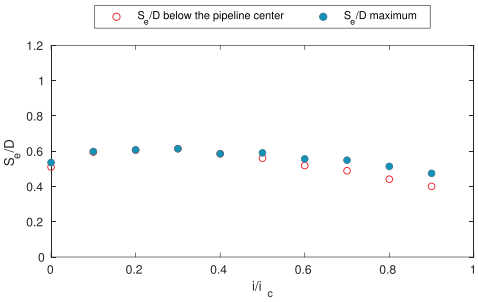

(a) Equilibrium scour depth with upward hydraulic gradients in the clear-water regime.

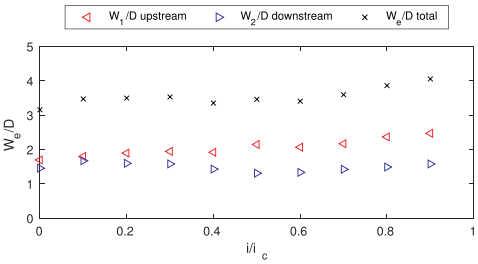

(b) Equilibrium scour width with upward hydraulic gradients in the clear-water regime.

Fig. 11. Equilibrium scour depth and width with upward hydraulic gradients in the clear-water regime.

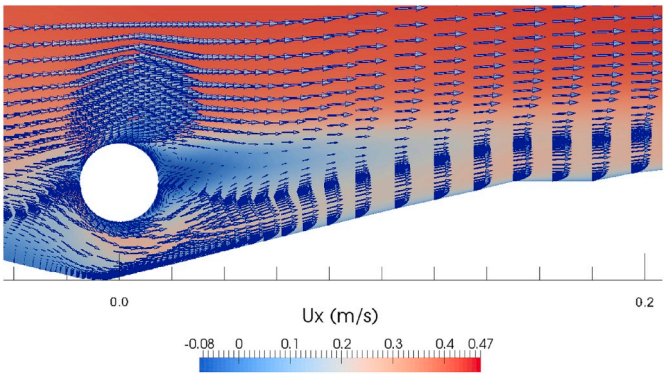

(a) Horizontal velocity field of the live-bed case with $i/i_c = 0.9$ ($t^* = 1.74$).

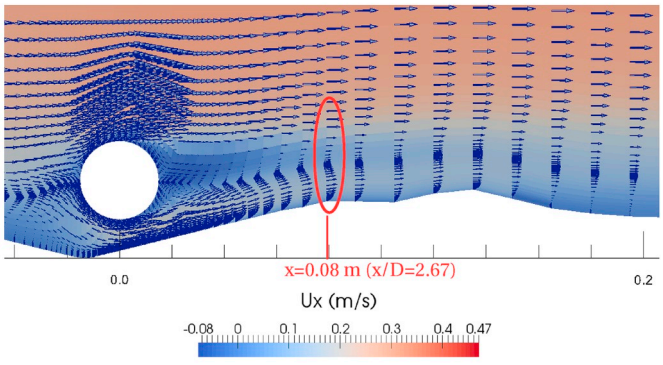

(b) Horizontal velocity field of the clear-water case with $i/i_c = 0.9$ ($t^* = 3.54$).

Fig. 12. Horizontal velocity field of cases with $i/i_c = 0.9$.

stress are changed. Meanwhile, the threshold of incipient sediment motion, i.e., the critical Shields parameter and the angle of repose of the sand particles are both reduced. To validate the present numerical model, first, the boundary layer velocity profile subjected to upward seepage has been validated against the experiments of Cheng and Chiew (1998) and Dey and Nath (2009). Good agreement has been achieved. Then, the fully-coupled hydrodynamic and morphologic scour model has been validated against the live-bed scour and clear-water scour experiments of Mao (1986). The present scour model has provided reasonably accurate predictions to the scour depths and the scour profiles.

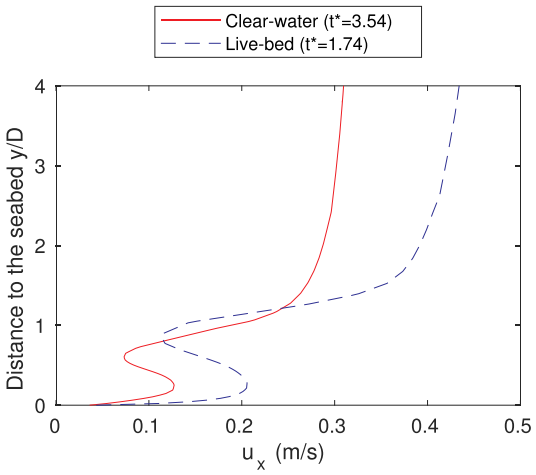

Fig. 13. Vertical distributions of the horizontal velocity near the seabed with $i/i_c = 0.9$ at $x = 0.08$ m ($x/D = 2.67$).

The validated numerical model has then been applied to investigate the scour beneath a submarine pipeline in the presence of upward seepage. The investigations have been based on the numerical cases of scour without seepage effects, i.e., the live-bed scour and the clear-water scour of Mao (1986). Nine levels of upward hydraulic gradients ($i/i_c = 0.1$–0.9) have been applied to the live-bed scour case and the clear-water scour case, respectively. The following conclusions can be drawn from the present study:

1. For the live-bed case in the present work, with upward hydraulic gradients $i/i_c = 0.1$–0.9, it is observed that the equilibrium scour depths are in the range of $S/D = 0.6 - 0.8$. During the initial stage of scour development, the scour depths with large upward hydraulic gradients, i.e., $i/i_c = 0.7$–0.9, are smaller than that with $i/i_c = 0$. However, after reaching equilibrium, the scour depths with $i/i_c = 0.7$–0.9 reach similar values as with $i/i_c = 0$. For small and medium upward hydraulic gradients, i.e., $i/i_c = 0.1$–0.6, the scour widths are similar, and are only slightly larger than with $i/i_c = 0$. As the upward hydraulic gradient increases from 0.7 to 0.9, the scour width increases more dramatically.
2. For the clear-water case in the present work, as the upward hydraulic gradient increases, the initial clear-water condition may turn into a live-bed condition, i.e., the far-field Shields parameter exceeds the critical Shields parameter, such as clear-water cases with $i/i_c = 0.4$–0.9 in the present study. It appears that the equilibrium scour depth decreases as i/i_c increases from 0.4 to 0.9. As i/i_c becomes higher, the location of the maximum S_e/D moves upstream of the pipeline center. For the clear-water cases with large upward hydraulic gradients, the equilibrium scour width increases with i/i_c. The upstream scour width increases with i/i_c, while the downstream scour width remains almost the same. Therefore, the total scour width W_e/D generally increases.
3. A general finding is that with upward seepage, the scour depth beneath the submarine pipeline may either increase or decrease, or remain similar in value. The scour width remains similar with small and medium hydraulic gradients and significantly increases with the existence of large upward hydraulic gradients.

It is noted that in the present parametric study, the relation between i

and v_s is based on a linear assumption. Also, for sediment particles with different properties, the empirical coefficient C_s for predicting the angle of repose subjected to upward seepage may differ. Nevertheless, the present numerical model, in terms of modeling the incoming flow velocity profile subjected to upward seepage and modeling the hydrodynamic- and morphologic-coupled scour beneath a submarine pipeline, has been validated. Therefore, it seems capable of providing practical predictions for engineering problems based on reasonable assumptions and parameters.

Declaration of competing interest

The authors would like to state that there is no conflict of interest for this manuscript.

Acknowledgment

This study was supported in part with computational resources provided by the Norwegian Metacenter for Computational Science (NOTUR), under Project No: NN9372K. The PhD project was financed by the Statoil Akademia program at the University of Stavanger.

Appendix A. Hydrodynamic and turbulence models

The present numerical model solves the incompressible unsteady Reynolds-averaged Navier-Stokes (URANS) equations with the $k-\omega$ turbulence model (Wilcox, 2006, 2008) as the closure. The equations governing the flow in the Cartesian coordinate system include a continuity equation and incompressible URANS equations:

$$\frac{\partial u_i}{\partial x_i}=0 \tag{30}$$

$$\frac{\partial u_i}{\partial t}+u_j\frac{\partial u_i}{\partial x_j}=-\frac{1}{\rho}\frac{\partial p}{\partial x_i}+\frac{\partial}{\partial x_j}\left[2\nu S_{ij}+\frac{\tau_{ij}}{\rho}\right]+F_i \tag{31}$$

where u_i are the mean velocities, x_i are the Cartesian coordinates, $\rho = 1000$ kg/m^3 is the fluid density, p is the pressure, $\nu = 10^{-6}$ m^2/s is the fluid kinematic viscosity, F_i is the external body force used to drive the initial 1DV flow (see Section 4.1), S_{ij} is the mean-strain-rate tensor defined as

$$S_{ij}=\frac{1}{2}\left(\frac{\partial u_i}{\partial x_j}+\frac{\partial u_j}{\partial x_i}\right) \tag{32}$$

τ_{ij} is the Reynolds stress tensor that defined according to the constitutive relation given by

$$\frac{\tau_{ij}}{\rho}=-\overline{u_i'u_j'}=2\nu_T S_{ij}-\frac{2}{3}k\delta_{ij} \tag{33}$$

where δ_{ij} is the Kronecker delta, k is the turbulent kinetic energy density expressed as

$$k=\frac{1}{2}\overline{u_i'u_i'} \tag{34}$$

and ν_T is the eddy viscosity. In the present work this is defined by

$$\nu_T=\frac{k}{\tilde{\omega}} \tag{35}$$

where the $\tilde{\omega}$ is defined by

$$\tilde{\omega}=\max\left\{\omega, C_{\lim}\sqrt{\frac{2S_{ij}S_{ij}}{\beta^*}}\right\}, C_{\lim}=\frac{7}{8} \tag{36}$$

The two-equation $k-\omega$ turbulence model is used in the present study as a closure for the URANS equations. The model includes the transport equation of the turbulent kinetic energy k and the specific dissipation rate ω (Wilcox, 2006):

$$\frac{\partial k}{\partial t}+u_j\frac{\partial k}{\partial x_j}=\frac{\tau_{ij}}{\rho}\frac{\partial u_i}{\partial x_j}-\beta^* k\omega+\frac{\partial}{\partial x_j}\left[\left(\nu+\sigma^*\frac{k}{\omega}\right)\frac{\partial k}{\partial x_j}\right] \tag{37}$$

$$\frac{\partial \omega}{\partial t}+u_j\frac{\partial \omega}{\partial x_j}=\alpha\frac{\omega}{k}\frac{\tau_{ij}}{\rho}\frac{\partial u_i}{\partial x_j}-\beta\omega^2+\frac{\sigma_d}{\omega}\frac{\partial k}{\partial x_j}\frac{\partial \omega}{\partial x_j}+\frac{\partial}{\partial x_j}\left[\left(\nu+\sigma\frac{k}{\omega}\right)\frac{\partial \omega}{\partial x_j}\right] \tag{38}$$

where

$$\sigma_d=H\left\{\frac{\partial k}{\partial x_j}\cdot\frac{\partial \omega}{\partial x_j}\right\}\sigma_{d0} \tag{39}$$

where $H\{\cdot\}$ denotes the Heaveside step function, which takes value 1 if the argument is positive and takes 0 otherwise. The standard closure coefficients are: $\alpha = 0.52$, $\beta = 0.0708$ (constant for two-dimensional problems), $\beta^* = 0.09$, $\sigma = 0.5$, $\sigma^* = 0.6$, $\sigma_{d0} = 0.125$.

References

Baykal, C., Sumer, B.M., Fuhrman, D.R., Jacobsen, N.G., Fredsøe, J., 2015. Numerical investigation of flow and scour around a vertical circular cylinder. Philos. Trans. R. Soc. A Math. Phys. Eng. Sci. 373, 20140104.

Bear, J., 2013. Dynamics of Fluids in Porous Media. Courier Corporation.

Brørs, B., 1999. Numerical modeling of flow and scour at pipelines. J. Hydraul. Eng. 125, 511–523.

Chao, J., Hennessy, P., 1972. Local scour under ocean outfall pipelines. Journal (Water Pollution Control Federation) 1443–1447.

Cheng, N.-S., Chiew, Y.-M., 1998. Modified logarithmic law for velocity distribution subjected to upward seepage. J. Hydraul. Eng. 124, 1235–1241.

Cheng, N.-S., Chiew, Y.-M., 1999. Incipient sediment motion with upward seepage. J. Hydraul. Res. 37, 665–681.

Chiew, Y.-M., 1991. Prediction of maximum scour depth at submarine pipelines. J. Hydraul. Eng. 117, 452–466.

Chiew, Y.-M., Parker, G., 1994. Incipient sediment motion on non-horizontal slopes. J. Hydraul. Res. 32, 649–660.

Dey, S., Nath, T.K., 2009. Turbulence characteristics in flows subjected to boundary injection and suction. J. Eng. Mech. 136, 877–888.

Dey, S., Singh, N.P., 2007. Clear-water scour depth below underwater pipelines. J. Hydro Environ. Res. 1, 157–162.

Engelund, F., Fredsøe, J., 1976. A sediment transport model for straight alluvial channels. Nord. Hydrol 7, 293–306.

Fredsøe, J., Deigaard, R., 1992. Mechanics of Coastal Sediment Transport Volume 3. World Scientific.

Fuhrman, D.R., Baykal, C., Sumer, B.M., Jacobsen, N.G., Fredsøe, J., 2014. Numerical simulation of wave-induced scour and backfilling processes beneath submarine pipelines. Coast. Eng. 94, 10–22.

Guo, Z., Jeng, D.-S., Zhao, H., Guo, W., Wang, L., 2019. Effect of seepage flow on sediment incipient motion around a free spanning pipeline. Coast. Eng. 143, 50–62.

Jacobsen, N.G., 2011. A Full Hydro-And Morphodynamic Description of Breaker Bar Development. Ph.D. thesis. Technical University of Denmark.

Jacobsen, N.G., Fredsoe, J., 2014. Formation and development of a breaker bar under regular waves. Part 2: sediment transport and morphology. Coast. Eng. 88, 55–68.

Jacobsen, N.G., Fredsoe, J., Jensen, J.H., 2014. Formation and development of a breaker bar under regular waves. Part 1: model description and hydrodynamics. Coast. Eng. 88, 182–193.

Larsen, B.E., Fuhrman, D.R., Sumer, B.M., 2016. Simulation of wave-plus-current scour beneath submarine pipelines. J. Waterw. Port, Coast. Ocean Eng. 142, 04016003.

Li, F., Cheng, L., 2000. Numerical simulation of pipeline local scour with lee-wake effects. Int. J. Offshore Polar Eng. 10.

Li, F., Cheng, L., 2001. Prediction of lee-wake scouring of pipelines in currents. J. Waterw. Port, Coast. Ocean Eng. 127, 106–112.

Li, Y., Ong, M.C., Fuhrman, D.R., Larsen, B.E., 2020. Numerical investigation of wave-plus-current induced scour beneath two submarine pipelines in tandem. Coast. Eng. 156, 103619.

Li, Y., Ong, M.C., Tang, T., 2018. Numerical analysis of wave-induced poro-elastic seabed response around a hexagonal gravity-based offshore foundation. Coast. Eng. 136, 81–95.

Liang, D., Cheng, L., Li, F., 2005. Numerical modeling of flow and scour below a pipeline in currents: Part ii. scour simulation. Coast. Eng. 52, 43–62.

Lu, Y., Chiew, Y.-M., 2007. Seepage effects on dune dimensions. J. Hydraul. Eng. 133, 560–563.

Lu, Y., Chiew, Y.-M., Cheng, N.-S., 2008. Review of seepage effects on turbulent open-channel flow and sediment entrainment. J. Hydraul. Res. 46, 476–488.

Luan, M., Qu, P., Jeng, D.-S., Guo, Y., Yang, Q., 2008. Dynamic response of a porous seabed–pipeline interaction under wave loading: soil–pipeline contact effects and inertial effects. Comput. Geotech. 35, 173–186.

Mao, Y., 1986. The Interaction between a Pipeline and an Erodible Bed. Institute of Hydrodynamics and Hydraulic Engineering. Technical University of Denmark.

Roulund, A., Sumer, B.M., Fredsøe, J., Michelsen, J., 2005. Numerical and experimental investigation of flow and scour around a circular pile. J. Fluid Mech. 534, 351–401.

Smith, H.D., Foster, D.L., 2005. Modeling of flow around a cylinder over a scoured bed. J. Waterw. Port, Coast. Ocean Eng. 131, 14–24.

Sumer, B.M., Fredsøe, J., 1990. Scour below pipelines in waves. J. Waterw. Port, Coast. Ocean Eng. 116, 307–323.

Sumer, B.M., Fredsøe, J., 1996. Scour Around Pipelines in Combined Waves and Current. Technical Report American Society of Mechanical Engineers, New York, NY (United States).

Sumer, B.M., Fredsøe, J., 2002. The Mechanics of Scour in the Marine Environment, vol. 17. World Scientific.

Sumer, B.M., Hatipoglu, F., Fredsøe, J., Sumer, S.K., 2006. The sequence of sediment behaviour during wave-induced liquefaction. Sedimentology 53, 611–629.

Wilcox, D.C., 2006. Turbulence Modeling for CFD, third ed., vol. 2. DCW industries La Canada, CA.

Wilcox, D.C., 2008. Formulation of the k-ω turbulence model revisited. AIAA J. 46, 2823–2838.

Ye, J., Jeng, D.-S., Wang, R., Zhu, C., 2013. A 3-D semi-coupled numerical model for fluid–structures–seabed-interaction (FSSI-CAS 3D): model and verification. J. Fluids Struct. 40, 148–162.

Zhang, C., Zhang, Q., Wu, Z., Zhang, J., Sui, T., Wen, Y., 2015. Numerical study on effects of the embedded monopile foundation on local wave-induced porous seabed response. Math. Probl. Eng. 2015.